
Reward Guided Latent Consistency Distillation

Jiachen Li¹, Weixi Feng¹, Wenhui Chen², William Yang Wang¹

¹UC Santa Barbara, ²University of Waterloo

¹{jiachen_li, weixifeng, william}@cs.ucsb.edu, ²wenhui.chen@uwaterloo.ca

Project Page: <https://rg-lcd.github.io>



Abstract

Latent Consistency Distillation (LCD) has emerged as a promising paradigm for efficient text-to-image synthesis. By distilling a latent consistency model (LCM) from a pre-trained teacher latent diffusion model (LDM), LCD facilitates the generation of high-fidelity images within merely 2 to 4 inference steps. However, the LCM’s efficient inference is obtained at the cost of the sample quality. In this paper, we propose compensating the quality loss by aligning LCM’s output with human preference during training. Specifically, we introduce Reward Guided LCD (RG-LCD), which integrates feedback from a reward model (RM) into the LCD process by augmenting the original LCD loss with the objective of maximizing the reward associated with LCM’s single-step generation. As validated through human evaluation, when trained with the feedback of a good RM, the 2-step generations from our RG-LCM are favored by humans over the 50-step DDIM [52] samples from the teacher LDM, representing a 25 times inference acceleration without quality loss.

As directly optimizing towards differentiable RMs can suffer from over-optimization, we overcome this difficulty by proposing the use of a latent proxy RM (LRM). This novel component serves as an intermediary, connecting our LCM with the RM. Empirically, we demonstrate that incorporating the LRM into our RG-LCD successfully avoids high-frequency noise in the generated images, contributing to both improved FID on MS-COCO [29] and a higher HPSv2.1 score on HPSv2 [64]’s test set, surpassing those achieved by the baseline LCM.

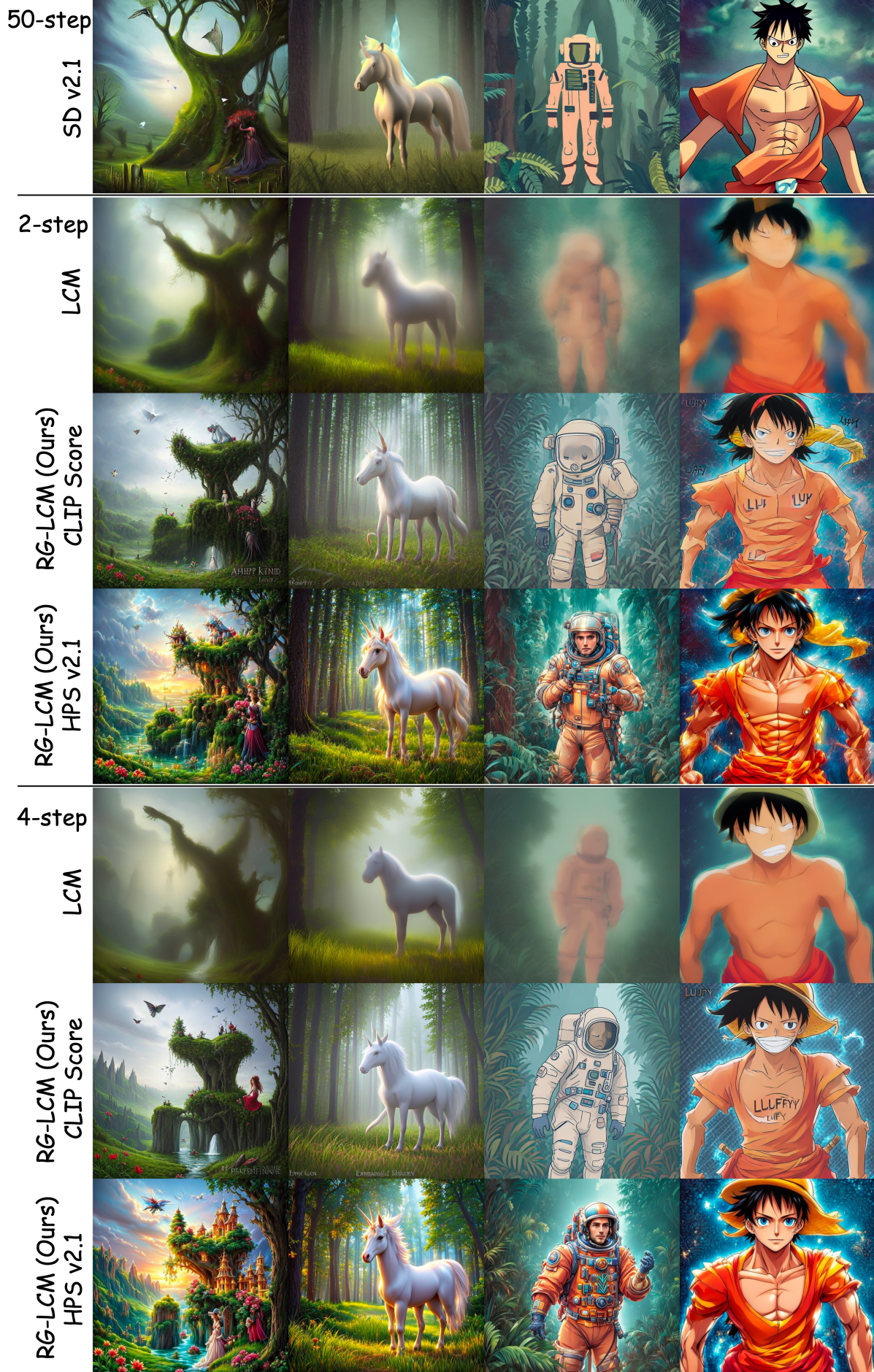


Figure 1: Even with merely 2-4 sampling steps, our RG-LCMs that learned from the CLIP Score and HPSv2.1 can produce high-quality images.

1 Introduction

In the realm of modern generative AI (GenAI) models, computational resources are typically allocated across three key areas: pretraining [5, 1, 28, 41, 43, 44, 3], alignment [73, 57, 39, 18, 7, 42], and inference [69, 13, 60, 49]. Normally, increasing the computational budget across these areas leads to improvements in sample quality. For instance, the most advanced text-to-image (T2I) models, such as DALLE-3 [3], ImageGen [44], and Stable Diffusion [43] are built from diffusion models (DMs) [51, 17, 54]. These models are pretrained on massive web-scale datasets [47, 6], aligned with human preference on curated high-quality images [8, 43], and benefit from the iterative sampling process of DMs.

However, DM’s iterative sampling requires performing 10 - 2000 sequential function evaluations (FEs) [17, 52], thus impeding rapid inference. While there have been many works proposed to address this issue [30, 31, 68, 46, 14, 37, 56], consistency model (CM) [56] emerges as a new family of GenAI model that facilitates fast sampling. A CM is trained to perform single-step generation while supporting multi-step sampling to trade compute for sample quality. We can distill a CM from a pretrained DM, a process known as consistency distillation (CD). For instance, Luo et al. distill a Latent CM (LCM) [35] from a pretrained Stable Diffusion [43], achieving high-fidelity image generation in just 2 to 4 FE steps. However, the sample quality of LCM is inherently constrained by the pretrained LDM’s capabilities [53]. Additionally, the reduced inference computational resources stemming from the limited number of FE steps compromise LCM’s sample quality.

In this paper, we aim to offset LCM’s sample quality by dedicating additional computational resources to the LCD process. As demonstrated by the recent success of large language models [2, 59], aligning a GenAI model to a reward model (RM) that mirrors human preferences dramatically improves its sample quality [39, 42]. We are thus motivated to integrate feedback from a differentiable RM into the LCD process. Facilitated by the fact that the LCD loss is calculated based on a single-step generation from the LCM, we propose to simultaneously train the LCM to maximize the reward associated with the generation, obviating the need for backpropagating gradients through the extensive denoising steps typically required in optimizing a DM [7, 66]. We dub our method *Reward Guided Latent Consistency Distillation* (RG-LCD). As evidenced by human evaluation, our RG-LCM significantly outperforms the LCM derived from standard LCD methods. Moreover, it even exceeds the capabilities of the pretrained LDM, which generates images using 50 DDIM steps, with just 2 FE steps, achieving a 25-fold increase in inference speed without compromising image quality.

While our RG-LCD is conceptually simple and already achieves impressive results, it can suffer from reward overestimation [22, 70] due to direct optimization with the gradient from the RM. As shown in the top row of Fig. 3, performing RG-LCD with ImageReward [66] causes high-frequency noise in the generated images. To tackle this challenge, we propose learning a latent proxy RM to serve as the intermediary that connects our LCM with the RM. Instead of directly optimizing towards the RM, we optimize the LCM towards the LRM while finetuning the LRM to match the preference of the expert RM in each RG-LCD iteration. This novel strategy allows us to optimize the expert RM indirectly, even allowing for learning from non-differentiable RMs. We empirically verify that incorporating the LRM into our RG-LCD successfully eliminates the high-frequency noise in the generated image, contributing to improved FID on MS-COCO [29] and a higher HPSv2.1 score on HPSv2’s test set [64], outperforming the baseline LCM.

In summary, our contributions are threefold:

- Introduction of RG-LCD framework, which incorporates feedback from an RM that mirrors human preference into the LCD process.
- Introduction of the LRM, which enables indirect optimization towards the RM, mitigating the issue of reward over-optimization.
- A 25 times inference acceleration over teacher LDM (Stable Diffusion v2.1) without compromising sample quality.

2 Related Work

Accelerating DM inference. Centering around DM’s SDE formulation [55], various methods have been proposed to accelerate the sampling process of a DM. For example, faster numerical

ODE solvers [52, 30, 31, 71, 10, 20] and distillation techniques [34, 45, 36, 72]. Recent advances explore enhancing the single-step generation quality by incorporating an adversarial loss [46] or by distillation [37]. Consistency Model [56] is also trained for single-step generation. We leverage this property and directly maximize the reward of this single-step generation given by a differentiable RM.

Consistency Model has emerged as a new family of GenAI model [56] that facilitates fast inference. While it is trained to perform single-step generation by mapping arbitrary points in the PF-ODE trajectory to the origin, CM also supports multi-step sampling, allowing for trading compute for better sample quality. A CM can be trained as a standalone GenAI model (consistency training). Recently, Song et al. proposed improved techniques [53] to support better consistency training. A CM can also be distilled from a pretrained DM. For instance, Luo et al. [35] learn an LCM by distilling from a pretrained Stable Diffusion [43]. We defer more technical details to Sec. 3.

Vision-and-language reward models. Motivated by the significant success of reinforcement from human feedback (RLHF), there have been many works delving into training an RM to mirror human preferences on a pair of text and image, including HPSv2 [64], ImageReward [66], PickScore [24]. These RMs are normally derived by finetuning a vision and language model, e.g., CLIP [41] and BLIP [27], on human preference data. Since these RMs are differentiable, our RG-LCD augments the standard LCD with the objective of maximizing the differentiable reward associated with its single-step during training.

Aligning DMs to Human preference has been extensively studied recently, including RL based methods [12, 40, 70] and reward finetuning methods [7, 66]. Recently, Diffusion-DPO [62] is proposed by extending DPO [42] to train DMs on preference data. Moreover, other works focus on modifying the training data distribution [65, 26, 11, 58, 8] to finetune DMs on visually appealing and textually cohered data. Additionally, alternative techniques [4, 48] re-caption pre-collected web images to enhance text accuracy. On the other hand, DOODL [63] is proposed to optimize the RM during inference time. However, its improvement is made at the cost of inference speed. While we also propose to directly finetune our model with the gradient given by an RM, finetuning an LCM during LCD is much simpler than finetuning a DM, as we only tackle the single-step generation, circumventing the need to pass gradients through DM’s complicated iterative sampling process.

3 Background

3.1 Diffusion Model

Diffusion models (DMs) [51, 54, 17, 38] progressively inject Gaussian noise into data in the forward process and sequentially denoise the data to create samples in the reverse denoising process. The forward process perturbs the original data distribution $p_{data}(\mathbf{x}) \equiv p_0(\mathbf{x}_0)$ to the marginal distributional $p_t(\mathbf{x}_t)$. From a continuous-time perspective, we can represent the forward process with a stochastic differential equation (SDE) [55, 21]

$$d\mathbf{x}_t = \boldsymbol{\mu}(t)\mathbf{x}_t dt + \sigma(t)d\mathbf{w}_t, \quad \mathbf{x}_0 \sim p_{data}(\mathbf{x}_0), \quad (1)$$

where $\boldsymbol{\mu}(\cdot)$ and $\sigma(\cdot)$ are the drift and diffusion coefficients respectively, and \mathbf{w}_t denotes the standard Wiener process. The reverse time SDE above corresponds to an ordinary differential equation (ODE)[55], named Probability Flow (PF-ODE), which is given by

$$d\mathbf{x}_t = \left[\boldsymbol{\mu}(t)\mathbf{x}_t - \frac{1}{2}\sigma(t)^2 \nabla \log p_t(\mathbf{x}_t) \right] dt, \quad \mathbf{x}_T \sim p_T(\mathbf{x}_T). \quad (2)$$

PF-ODE’s solution trajectories sampled at t are distributed the same as $p_t(\mathbf{x}_t)$. Empirically, we learn a denoising model $\epsilon_\theta(\mathbf{z}_t, t)$ to fit $-\nabla \log p_t(\mathbf{x}_t)$ (score function) via score matching [19, 54, 17]. During sampling, we start from the sample $\mathbf{x}_T \sim \mathcal{N}(\mathbf{0}, \tilde{\sigma}^2 \mathbf{I})$ and follow the empirical PF-ODE below

$$d\mathbf{x}_t = \left[\boldsymbol{\mu}(t)\mathbf{x}_t + \frac{1}{2}\sigma(t)^2 \epsilon_\theta(\mathbf{z}_t, t) \right] dt, \quad \mathbf{x}_T \sim \mathcal{N}(\mathbf{0}, \tilde{\sigma}^2 \mathbf{I}). \quad (3)$$

In this paper, we focus on conditional LDM that operates on the image latent space \mathcal{Z} and includes a text prompt \mathbf{c} passed to the denoising model $\epsilon_\theta(\mathbf{z}_t, \mathbf{c}, t)$, where $\mathbf{z}_t = \mathcal{E}(\mathbf{x}_t) \in \mathcal{Z}$ is encoded by a VAE [23] encoder \mathcal{E} . Moreover, we utilize Classifier-Free Guidance (CFG) [16] to improve the quality

of conditional sampling by replacing the noise prediction with a linear combination of conditional and unconditional noise prediction for denoising, i.e., $\tilde{\epsilon}_\theta(\mathbf{z}_t, \omega, \mathbf{c}, t) = (1 + \omega)\epsilon_\theta(\mathbf{z}_t, \mathbf{c}, t) - \omega\epsilon_\theta(\mathbf{z}, \emptyset, t)$, where ω is the CFG scale.

3.2 Consistency Model

Consistency model (CM) [56] is proposed to facilitate efficient generation. At its core, CM learns a consistency function $\mathbf{f} : (\mathbf{x}_t, t) \mapsto \mathbf{x}_\epsilon$ that can map any point \mathbf{x}_t on the same PF-ODE trajectory to the trajectory’s origin, where ϵ is a fixed small positive number. Learning the consistency function involves enforcing the *self-consistency* property

$$\mathbf{f}(\mathbf{x}_t, t) = \mathbf{f}(\mathbf{x}'_t, t'), \forall t, t' \in [\epsilon, T], \quad (4)$$

where \mathbf{x}_t and \mathbf{x}'_t belong to the same PF-ODE. The consistency function \mathbf{f} is modeled with a CM \mathbf{f}_θ . To ensure $\mathbf{f}_\theta(\mathbf{x}, \epsilon) = \mathbf{x}$, \mathbf{f}_θ is parameterized as

$$\mathbf{f}_\theta(\mathbf{x}, t) = c_{\text{skip}}(t)\mathbf{x} + c_{\text{out}}(t)F_\theta(\mathbf{x}, t), \quad (5)$$

where $c_{\text{skip}}(t)$ and $c_{\text{out}}(t)$ are differentiable functions with $c_{\text{skip}}(\epsilon) = 1$ and $c_{\text{out}}(\epsilon) = 0$, and F_θ is a neural network. We can learn a CM \mathbf{f}_θ by distilling from a pretrained DM, known as *consistency distillation* (CD) [56]. The CD loss is given by

$$L_{\text{CD}}(\theta, \theta^-; \Phi) = \mathbb{E}_{\mathbf{x}, t} \left[d \left(\mathbf{f}_\theta(\mathbf{x}_{t_{n+1}}, t_{n+1}), \mathbf{f}_{\theta^-}(\hat{\mathbf{x}}_{t_n}^\phi, t_n) \right) \right]. \quad (6)$$

where $d(\cdot, \cdot)$ measures the distance between two samples. θ^- is the parameter of the target CM \mathbf{f}_{θ^-} , updated by the exponential moving average (EMA) of θ , i.e., $\theta^- \leftarrow \text{stop_grad}(\mu\theta + (1 - \mu)\theta^-)$. $\hat{\mathbf{x}}_{t_n}^\phi$ is an estimation of \mathbf{x}_{t_n} from $\mathbf{x}_{t_{n+1}}$ using the one-step ODE solver Φ :

$$\hat{\mathbf{x}}_{t_n}^\phi \leftarrow \mathbf{x}_{t_{n+1}} + (t_n - t_{n+1})\Phi(\mathbf{x}_{t_{n+1}}, t_{n+1}; \phi). \quad (7)$$

Note that the parameter ϕ corresponds to the parameter of the pretrained DM, which is used to construct the ODE solver Φ . We include the algorithm for sampling from a CM in Appendix B.

3.3 Latent Consistency Model

Luo et al. [35] extends CM to work on latent space \mathcal{Z} and focuses on conditional generation. Specifically, a Latent CM (LCM) $\mathbf{f}_\theta : (\mathbf{z}_t, \omega, \mathbf{c}, t) \mapsto \mathbf{z}_0$ is trained to minimize the LCD loss

$$L_{\text{LCD}}(\theta, \theta^-; \Psi) = \mathbb{E}_{\mathbf{z}, \mathbf{c}, \omega, n} \left[d \left(\mathbf{f}_\theta(\mathbf{z}_{t_{n+k}}, \omega, \mathbf{c}, t_{n+k}), \mathbf{f}_{\theta^-}(\hat{\mathbf{z}}_{t_n}^{\Psi, \omega}, \omega, \mathbf{c}, t_n) \right) \right], \quad (8)$$

where $\hat{\mathbf{z}}_{t_n}^{\Psi, \omega}$ is an estimate of \mathbf{z}_{t_n} obtained by the numerical augmented PF-ODE solver Ψ and k is skipping interval.

$$\hat{\mathbf{z}}_{t_n}^{\Psi, \omega} \leftarrow \mathbf{z}_{t_{n+k}} + (1 + \omega)\Psi(\mathbf{z}_{t_{n+k}}, t_{n+k}, t_n, \mathbf{c}; \psi) - \omega\Psi(\mathbf{z}_{t_{n+k}}, t_{n+k}, t_n, \emptyset; \psi). \quad (9)$$

In this paper, we use DDIM [52] as the ODE solver Ψ to distill from a pretrained Stable Diffusion [43] and refer interested readers to the original LCM paper for formula of the DDIM solver. We use huber loss as our distance function $d(\cdot, \cdot)$.

4 Reward Guided Latent Consistency Distillation

In this section, we start by presenting the core components of our RG-LCD framework, which augments the standard LCD loss (8) with an objective towards maximizing a differentiable RM, as shown in Fig. 2 (Sec. 4.1). We then motivate the development of a latent proxy RM (LRM) to support indirect RM optimization by illustrating the risk of suffering from reward over-optimization when directly optimizing towards the RM with a gradient-based method. Following this, we then detail the procedure to pretrain and finetune the LRM to match the preference of the RGB-based RM during RG-LCD (Sec. 4.2).

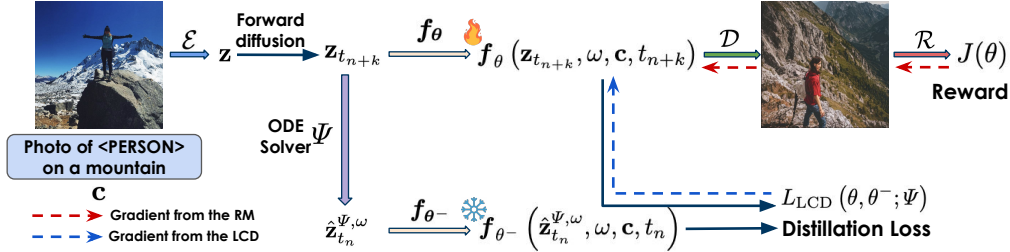


Figure 2: Overview of our RG-LCD. We integrate feedback from a differentiable RM into the standard LCD procedures by training the LCM to maximize the reward associated with its single-step generation.

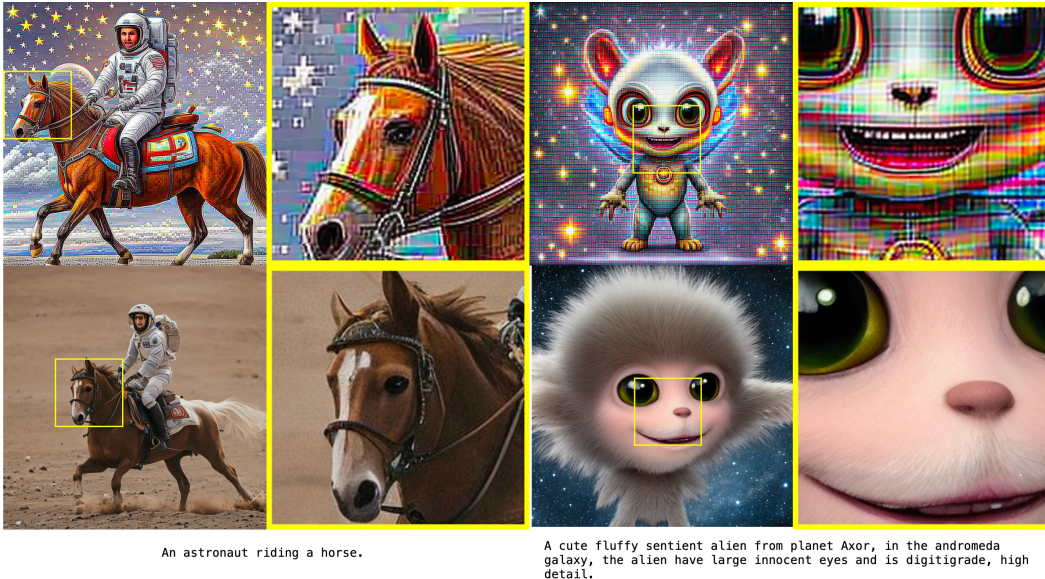


Figure 3: (Top) Optimizing the RG-LCM with the gradient from ImageReward [66] results in high-frequency noise in the generated images. (Bottom) Indirectly optimizing the ImageReward through the latent proxy RM eliminates the high-frequency noise, avoiding reward over-optimization.

4.1 RG-LCD with Differentiable RMs

Recall that each LCD iteration samples a timestep t_{n+k} , and construct the noisy latent $\mathbf{z}_{t_{n+k}}$ by perturb the image latent $\mathbf{z} = \mathcal{E}(\mathbf{x})$ with a Gaussian noise, given a sampled CFG scale ω and text prompt \mathbf{c} . As the LCM f_{θ} maps the $\mathbf{z}_{t_{n+k}}$ to the PF-ODE origin $\hat{\mathbf{z}}_0 = f_{\theta}(\mathbf{z}_{t_{n+k}}, \omega, \mathbf{c}, t_{n+k})$, we construct the following objective to maximize the reward associated with $\mathcal{D}(\hat{\mathbf{z}}_0)$

$$J(\theta) = \mathbb{E}_{\mathbf{z}, \mathbf{c}, \omega, n} [\mathcal{R}(\mathcal{D}(f_{\theta}(\mathbf{z}_{t_{n+k}}, \omega, \mathbf{c}, t_{n+k}))), \mathbf{c}], \quad (10)$$

where \mathcal{R} is a differentiable RM that calculates the rewards associated with a pair of text and image. We define the training loss of our RG-LCD by a linear combination of the LCD loss in (8) and $J(\theta)$ with a weighting parameter β

$$L_{\text{RG-LCD}}(\theta, \theta^-; \Psi) = L_{\text{LCD}}(\theta, \theta^-; \Psi) - \beta J(\theta) \quad (11)$$

Appendix B includes pseudo-codes for our RG-LCD training.

4.2 RG-LCD with a Latent Proxy RM

When training the LCM f_θ towards $J(\theta)$ with a gradient-based method, we may suffer from the issue of reward over-optimization. As shown in the top row of Fig. 3, performing RG-LCD with ImageReward [66] causes high-frequency noise in the generated images. To mitigate this issue, we propose learning a latent proxy RM \mathcal{R}_σ^L to serve as an intermediary to connect f_θ and the RGB-based RM \mathcal{R}^E . Specifically, we train f_θ to optimize the reward given by \mathcal{R}_σ^L while simultaneously finetuning the \mathcal{R}_σ^L to match the preference given by the expert RM \mathcal{R}^E that process RGB images.

Ideally, the LRM \mathcal{R}_σ^L should be capable of accessing the text-image pair even at the beginning of RG-LCD. We thus initialize \mathcal{R}_σ^L with a pretrained CLIP [41] text encoder, complemented by pretraining its latent encoder from scratch. This latent encoder is pretrained following the same methodology used for CLIP visual encoders, ensuring it aligns effectively with the text encoder’s representation.

After pretraining, we finetune \mathcal{R}_σ^L to match the preference of \mathcal{R}^E . Note that we do not need to assume a differentiable \mathcal{R}^E anymore, allowing us to learn from the feedback from a wider range of RGB-based RM, e.g., LLMscore [33], VIEScore [25] and DA-score [50]. Given $\mathbf{z}_0 = \mathbf{z}$, $\mathbf{z}_1 = f_\theta(\mathbf{z}_{t_{n+k}}, \omega, \mathbf{c}, t_{n+k})$, and $\mathbf{z}_2 = f_{\theta^-}(\mathbf{z}_{t_n}, \omega, \mathbf{c}, t_n)$ in each RG-LCD iteration, we train the the LRM \mathcal{R}_σ^L to match the \mathcal{R}^E ’s preference by

$$L_{\text{RM}}(\sigma) = \mathbb{E}_{\mathbf{z}, \mathbf{c}, \omega, n} \left[\sum_{i=0}^1 \sum_{j=i+1}^2 D_{\text{KL}}(P_{i,j}^\sigma \parallel \text{stop_grad}(Q_{i,j})) \right], \text{ where} \quad (12)$$

$$P_{i,j}^\sigma(k) = \frac{s_\sigma^L(\mathbf{z}_k, \mathbf{c})}{s_\sigma^L(\mathbf{z}_i, \mathbf{c}) + s_\sigma^L(\mathbf{z}_j, \mathbf{c})}, Q_{i,j}(k) = \frac{s^E(\mathbf{z}_k, \mathbf{c})}{s^E(\mathbf{z}_i, \mathbf{c}) + s^E(\mathbf{z}_j, \mathbf{c})}, k \in \{i, j\}$$

$$s_\sigma^L(\mathbf{z}, \mathbf{c}) = \exp(\mathcal{R}_\sigma^L(\mathbf{z}, \mathbf{c}) / \tau_L), s^E(\mathbf{z}, \mathbf{c}) = \exp(\mathcal{R}^E(\mathcal{D}(\mathbf{z}), \mathbf{c}) / \tau_E)$$

τ_L and τ_E are temperature parameters. $L_{\text{RM}}(\sigma)$ also supports matching a \mathcal{R}^E that only output preference over two images. In this case, we can set τ_E to a small positive number and only give a non-zero positive reward to the sample favored by the expert. Moreover, since $\mathbf{z}_0 = \mathbf{z}$ corresponds to the latent of a real image, we can adjust $Q_{0,j}$ to prefer $k = 0$ with a increased likelihood.

While calculating $s^E(\mathbf{z}, \mathbf{c})$ still requires decoding the latent, the application of the `stop_grad` operation eliminates the need for gradient transmission through \mathcal{D} , leading to a substantial reduction in memory usage. Moreover, optimizing \mathcal{R}_σ^L with $L_{\text{RM}}(\sigma)$ is independent from optimizing f_θ with $L_{\text{RG-LCD}}$. Therefore, we can use a smaller batch size to optimize \mathcal{R}_σ^L without affecting the batch size used to optimize f_θ .

In essence, our LRM acts as an proxy connecting the LCM f_θ and the expert RM \mathcal{R}^E . As we will show Sec. 5.2, using this indirect feedback from the expert mitigate the issue of reward over-optimization, avoiding high-frequency noise in the generated images.

5 Experiment

We perform thorough experiments to demonstrate the effectiveness of our RG-LCD. Sec. 5.1 conducts human evaluation to compare the performance of our methods with baselines. Sec. 5.2 further increases the experiment scales to experiment with a wider array of RMs with automatic metrics. By connecting both evaluation results, we identify problems with the current RMs. Finally, Sec. 5.3 conducts ablation studies on critical design choices.

Settings Our training are conducted on the CC12M datasets [6], as the LAION-Aesthetics datasets [47] used by the original LCM [35] are no longer accessible¹. We distill our LCM from the Stable Diffusion-v2.1 [43] by training for 10K iterations on 8 NVIDIA A100 GPUs without gradient accumulation and set the batch size to reach the maximum capacity of our GPUs. We follow the hyperparameter settings listed in the diffusers [61] library by setting learning rate $1e - 6$, EMA rate $\mu = 0.95$ and the guidance scale range $[\omega_{\min}, \omega_{\max}] = [5, 15]$. As mentioned in Sec. 3.3, we use DDIM [52] as our ODE solver Ψ with a skipping step $k = 20$. We include more training details in Appendix A.

¹<https://laion.ai/notes/laion-maintenance>

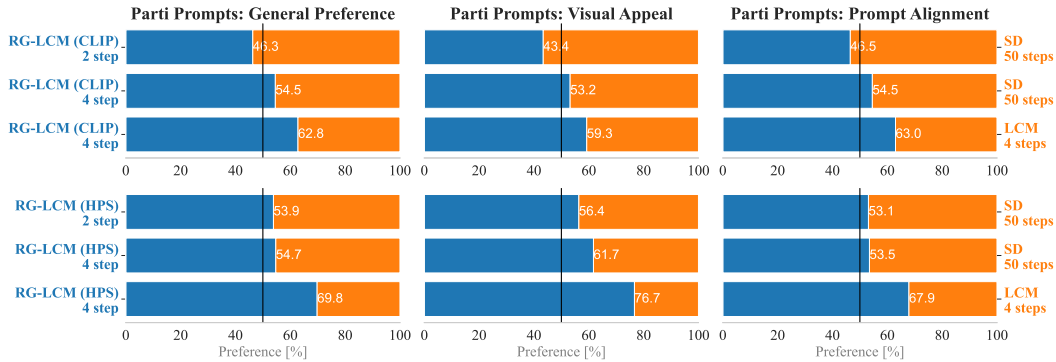


Figure 4: Human evaluation results on the PartiPrompt (1632 prompts) across three evaluation questions. Top row evaluates the RG-LCM (CLIP). Bottom row evaluates the RG-LCM (HPS).

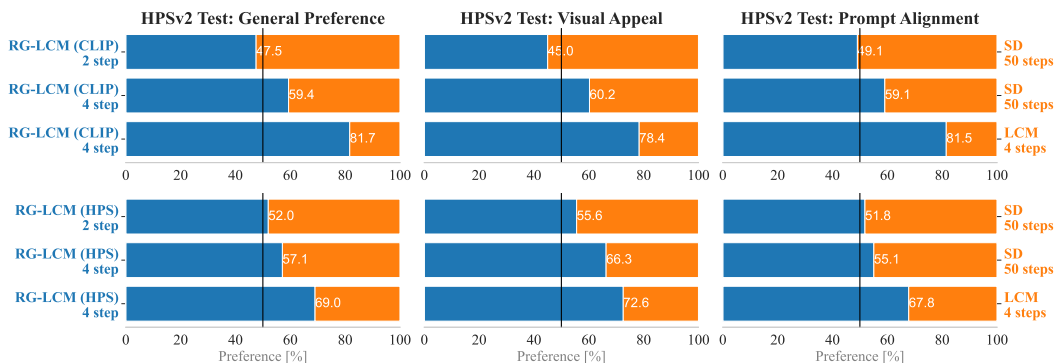


Figure 5: Human evaluation results on the HPSv2 test set (3200 prompts) across three evaluation questions. Top row evaluates the RG-LCM (CLIP). Bottom row evaluates the RG-LCM (HPS).

5.1 Evaluating RG-LCD with Human

We train RG-LCM (HPS) and RG-LCM (CLIP) utilizing feedback from HPSv2.1 [64] and CLIP-Score [41], respectively. CLIPScore evaluates the relevance between text and images, whereas HPSv2.1, derived by fine-tuning CLIPScore with human preference data, is expected to mirror human preferences more accurately. We choose the teacher LDM (Stable Diffusion v2.1) and a standard LCM distilled from the same teacher LDM as the baseline methods. To demonstrate the efficacy of our methods, we compare the performance of our RG-LCMs over 2-step and 4-step generations against the 50-step generations from the teacher LDM and evaluate the 4-step generation quality of our RG-LCMs against the standard LCM.

We follow a similar evaluation protocol as in [62] to generate images by conditioning on prompts from Partiprompt [67] (1632 prompts) and of HPSv2’s test set [64] (3200 prompts). We hire labelers from Amazon Mechanical Turk for a head-to-head comparison of images based on three criteria: Q1 General Preference (Which image do you prefer given the prompt?), Q2 Visual Appeal (Which image is more visually appealing, irrespective of the prompt?), and Q3 Prompt Alignment (Which image better matches the text description?).

The full human evaluation results in Fig. 4 and 5 show that the 2-step generations from RG-LCM (CLIP) are generally preferred (Q1) over the 50-step generations of the teacher LDM in both prompt sets, representing a 25-fold acceleration in inference speed. Even with CLIPScore feedback, the 4-step generations from our RG-LCM are generally preferred (Q1) over the baseline methods. This indicates a noteworthy achievement, given that CLIPScore does not train on human preference data. Surprisingly, on the HPSv2 prompt set, the 4-step generations from the RG-LCM (CLIP) are more preferred (59.4% against 50-step DDIM samples from SD and 81.7% against 4-step LCM samples)

Models	NFEs	Human Preference Score v2.1 \uparrow				FID-30K \downarrow
		Anime	Photo	Concept-Art	Paintings	MS-COCO
LCM	4	22.40	19.17	18.86	20.55	19.05
Stable Diffusion v2.1	50	25.66	24.37	24.58	25.72	12.66
RG-LCM (CLIP)	2	26.32	25.01	25.27	26.71	18.06
RG-LCM (CLIP)	4	27.80	26.92	27.04	28.11	19.22
RG-LCM (Pick)	2	26.44	28.26	28.24	29.04	22.84
RG-LCM (Pick)	4	27.33	29.42	29.29	30.26	22.02
RG-LCM (Pick) + LRM	2	23.82	21.31	21.90	22.99	15.91
RG-LCM (Pick) + LRM	4	25.17	23.06	22.90	24.87	16.27
RG-LCM (ImgRwd)	2	29.65	31.03	31.15	32.00	<u>32.12</u>
RG-LCM (ImgRwd)	4	30.26	31.83	31.88	32.73	<u>42.69</u>
RG-LCM (ImgRwd) + LRM	2	25.64	25.61	25.82	25.75	17.57
RG-LCM (ImgRwd) + LRM	4	26.84	26.72	26.72	27.30	17.20
RG-LCM (HPS)	2	30.85	33.66	33.35	33.66	24.04
RG-LCM (HPS)	4	31.83	34.84	34.43	34.75	25.11
RG-LCM (HPS) + LRM	2	24.22	22.43	22.94	23.16	15.60
RG-LCM (HPS) + LRM	4	25.60	24.24	24.08	25.14	15.25

Table 1: Evaluation of our RG-LCMs on the HPSv2 test prompts and MS-COCO datasets. NFEs denotes the number of function evaluation during inference. We train RG-LCMs with CLIPScore, PickScore, ImageReward (ImgRwd) and HPSv2.1. We employ the HPSv2.1 to evaluate the generations on HPSv2 Benchmark’s test set. We calculate the FID of the generations on the MS-COCO. Except trained with CLIPScore, our RG-LCMs achieve better HPSv2.1 scores on HPSv2 test prompts at the expense of higher FIDs on MS-COCO. Integrating a LRM into our RG-LCD process allows for simultaneously improvement on HPSv2.1 scores on HPSv2 test prompts and FID on MS-COCO against the baseline LCM.

compared to the 4-step generations of the RG-LCM (CLIP) (57.1% against 50-step DDIM samples from SD, and 69.0% against 4-step LCM samples).

To investigate this phenomenon, we observe that both RG-LCMs score similarly in General Preference (Q1) and Prompt Alignment (Q3). However, the RG-LCM (CLIP) is rated slightly lower in Visual Appeal (Q2) than in the other criteria, whereas the RG-LCM (HPS) is rated significantly higher for Q2 compared to Q1 and Q3. This distinction highlights that CLIPScore’s primary contribution is enhancing text-image alignment, whereas an RM like HPSv2.1 particularly focuses on improving visual quality. Thus, when over-optimizing towards HPSv2.1, the RG-LCM (HPS) can be biased in generating visually appealing samples by sacrificing prompt alignment.

5.2 Evaluating RG-LCD with Automatic Metrics

In this section, we further train RG-LCD (ImgRwd) and RG-LCD (Pick) by leveraging feedback from ImageReward [66] and PickScore [24]. Both of these RMs are trained on human preference data. We will use automatic metrics to perform a large-scale evaluation of the performance of different models. As we have human evaluation results for RG-LCD (HPS) and RG-LCD (CLIP), we can also evaluate the quality of the automatic metrics. For each RG-LCD, we collect their 2-step and 4-step generations by conditioning on prompts from HPSv2’s test set and measuring the HPSv2.1 score associated with the samples. To comprehensively understand the sample quality from different models, we further generate images conditioned on the prompts of MS-COCO [29] and measure their Fréchet Inception Distance (FID) to the ground truth images.

Table 1 presents the full evaluation results with the automatic metrics. Except for RG-LCM (CLIP), all the other RG-LCMs achieve higher HPSv2.1 scores than the baseline LCM but at the expense of higher FID values on the MS-COCO dataset. Specifically, the RG-LCM (ImgRwd) model exhibits a notably high FID value, yet it still secures an impressive HPSv2.1 score when evaluated on HPSv2 test prompts. The elevated FID value aligns with expectations, as Figure 3 illustrates that optimization






















	LCM	RG-LCM					
A dog is reading a thick book							
Mountains range with waterfall, purple haze, art by greg rutkowski and magali villeneuve, artstation.							
A photo of beautiful mountain with realistic sunset and blue lake, highly detailed, masterpiece							
		HPSv2.1 $\beta = 1$	HPSv2.1 $\beta = 100$	PickScore $\beta = 5$	PickScore $\beta = 50$	CLIPScore $\beta = 5$	CLIPScore $\beta = 100$

Figure 6: Ablating the reward scale β for different reward functions. All samples are generated with 4 steps. We observe that over-optimizing RMs that trained with preference data prioritizes visual appeal over text alignment. In contrast, over-optimizing CLIPScore compromises visual attractiveness in favor of text alignment.

directed towards ImageReward tends to introduce a significant amount of high-frequency noise into the generated images. Surprisingly, these high-frequency noises do not adversely affect the HPSv2.1 scores. Furthermore, the HPSv2.1 scores do not capture the human preference for the 4-step samples from RG-LCM (CLIP) by giving the highest score to RG-LCM (HPS)'s 4-step samples, contrary to what is depicted in human evaluation shown in Fig. 5.

These observations suggest that the HPSv2.1 score, as a metric, has limitations and requires further refinement. We conjecture that the *Resize* operation, which happens during the preprocessing phase, causes the HPSv2.1 model to overlook the high-frequency noise during reward calculation. As illustrated in Fig. 3, the high-frequency noise becomes less perceptible when images are reduced in size. Although resizing operations enhance efficiency in tasks such as image classification [32, 9, 15] and facilitate high-level text-image understanding [41], they prevent the model from capturing critical visual nuances that are vital for accurately reflecting human preferences. Consequently, we advocate for future RMs to **exclude the *Resize* operation**. One potential approach could involve training an LRM, as in our paper, to learn human preferences in the latent space, circumventing the need for resizing images.

Connecting Table 1 with the human evaluation results in Fig. 5 suggests that images that achieve a high HPSv2.1 score and a low FID on MS-COCO are more aligned with human preferences. Moreover, this desirable outcome can be accomplished by integrating an LRM into our RG-LCD. Although these correlations do not imply causality, they underscore the potential benefits of utilizing an LRM in the RG-LCD process. As depicted in the bottom row in Fig. 3, the images generated by RG-LCM (ImgRwd) that integrates an LRM do not suffer from high-frequency noise, contributing to their improved FID on MS-COCO. In Appendix C, we include additional samples for each RG-LCM in Table 1.

5.3 Ablation Study

Ablation on the reward scale β . We use the hyperparameter β to determine the optimization strength towards the RM. We are especially interested in the impact of an extremely large β , which can lead to reward over-optimization [22]. We already know that over-optimizing the ImageReward can lead to the introduction of high-frequency noise in the generated images. To expand our understanding, we conduct experiments a wider array of RMs including HPSv2.1, PickScore and CLIPScore and evaluate whether over-optimizing these RMs will also leads to similar high-frequency noise.



Figure 7: Ablation study on the number of training iterations. We generate all samples with 4 steps. We observe that RG-LCM, which learns from an RM that prioritizes visual appeal, can generate high-quality images with fewer training iterations.

The results in Figure 6 reveal that an extremely large β value does not introduce the high-frequency noise when using HPSv2.1, PickScore, and CLIPScore, even though all these metrics resize input images to 224×224 pixels as in ImageReward. Notably, over-optimization of HPSv2.1 leads to generating images with repetitive objects as described in the text prompts and increases color saturation. Conversely, over-optimization of PickScore tends to result in images with more muted colors. On the other hand, excessive optimization of CLIPScore results in images where the text prompts are visibly incorporated into the imagery. These findings align with the discussions in Sec. 5.1, suggesting that optimizing towards a preference-trained RM generally prioritizes visual appeal over text alignment. In contrast, over-optimizing CLIPScore compromises visual attractiveness in favor of text alignment. We include additional image samples in Appendix C.

Ablation on the training iterations. In total, we train each RG-LCM for 10K iterations. We take checkpoints from 1K, 2K, 4K, and 10K iterations and sample images with the same prompts and seeds. We can observe performing RG-LCD with RMs that facilitate the visual appeal of the generated images also results in fast training, as the checkpoint at the 2K iterations can already produce high-quality images. In contrast, the images generated by RG-LCM (CLIP) still generate blurry images after training for 2K iterations.

6 Conclusion

In this paper, we introduce RG-LCD, a novel strategy that integrates feedback from an RM into the LCD process. The RG-LCM learned via our method enjoys better sample quality while facilitating fast inference, benefiting from additional computational resources allocated to align with human preferences. By evaluating using prompts from the HPSv2 [64] test set and PartiPrompt [67], we empirically show that humans favor the 2-step generations of our RG-LCD (HPS) over the 50-step DDIM generations of the teacher LSM. This represents a 25-fold increase in terms of inference speed without a loss in quality. Moreover, even when using CLIPScore—a model not fine-tuned on human preferences—our method’s 4-step generations still surpass the 50-step DDIM generations from the teacher LDM.

We also identify that directly optimizing towards an imperfect RM, e.g., ImageReward, can cause high-frequency noise in generated images. To reconcile the issue, we propose integrating an LRM into the RG-LCD framework. Notably, our methods not only prevents reward over-optimization but also avoids passing gradients through the VAE decoder and facilitates learning from non-differentiable RMs.

References

- [1] J. Achiam, S. Adler, S. Agarwal, L. Ahmad, I. Akkaya, F. L. Aleman, D. Almeida, J. Altenschmidt, S. Altman, S. Anadkat, et al. Gpt-4 technical report. *arXiv preprint arXiv:2303.08774*, 2023.
- [2] J. Achiam, S. Adler, S. Agarwal, L. Ahmad, I. Akkaya, F. L. Aleman, D. Almeida, J. Altenschmidt, S. Altman, S. Anadkat, et al. Gpt-4 technical report. *arXiv preprint arXiv:2303.08774*, 2023.
- [3] J. Betker, G. Goh, L. Jing, T. Brooks, J. Wang, L. Li, L. Ouyang, J. Zhuang, J. Lee, Y. Guo, et al. Improving image generation with better captions. *Computer Science*. <https://cdn.openai.com/papers/dall-e-3.pdf>, 2(3):8, 2023.
- [4] J. Betker, G. Goh, L. Jing, TimBrooks, J. Wang, L. Li, LongOuyang, JuntangZhuang, JoyceLee, YufeiGuo, WesamManassra, PrafullaDhariwal, CaseyChu, YunxinJiao, and A. Ramesh. Improving image generation with better captions. 2023. URL <https://api.semanticscholar.org/CorpusID:264403242>.
- [5] T. Brown, B. Mann, N. Ryder, M. Subbiah, J. D. Kaplan, P. Dhariwal, A. Neelakantan, P. Shyam, G. Sastry, A. Askell, et al. Language models are few-shot learners. *Advances in neural information processing systems*, 33:1877–1901, 2020.
- [6] S. Changpinyo, P. Sharma, N. Ding, and R. Soricut. Conceptual 12m: Pushing web-scale image-text pre-training to recognize long-tail visual concepts. In *Proceedings of the IEEE/CVF Conference on Computer Vision and Pattern Recognition*, pages 3558–3568, 2021.
- [7] K. Clark, P. Vicol, K. Swersky, and D. J. Fleet. Directly fine-tuning diffusion models on differentiable rewards. *arXiv preprint arXiv:2309.17400*, 2023.
- [8] X. Dai, J. Hou, C.-Y. Ma, S. Tsai, J. Wang, R. Wang, P. Zhang, S. Vandenhende, X. Wang, A. Dubey, et al. Emu: Enhancing image generation models using photogenic needles in a haystack. *arXiv preprint arXiv:2309.15807*, 2023.
- [9] J. Deng, W. Dong, R. Socher, L.-J. Li, K. Li, and L. Fei-Fei. Imagenet: A large-scale hierarchical image database. In *2009 IEEE conference on computer vision and pattern recognition*, pages 248–255. Ieee, 2009.
- [10] T. Dockhorn, A. Vahdat, and K. Kreis. Genie: Higher-order denoising diffusion solvers. *Advances in Neural Information Processing Systems*, 35:30150–30166, 2022.
- [11] H. Dong, W. Xiong, D. Goyal, R. Pan, S. Diao, J. Zhang, K. Shum, and T. Zhang. Raft: Reward ranked finetuning for generative foundation model alignment. *arXiv preprint arXiv:2304.06767*, 2023.
- [12] Y. Fan, O. Watkins, Y. Du, H. Liu, M. Ryu, C. Boutilier, P. Abbeel, M. Ghavamzadeh, K. Lee, and K. Lee. Reinforcement learning for fine-tuning text-to-image diffusion models. *Advances in Neural Information Processing Systems*, 36, 2024.
- [13] X. Feng, Z. Wan, M. Wen, Y. Wen, W. Zhang, and J. Wang. Alphazero-like tree-search can guide large language model decoding and training. *arXiv preprint arXiv:2309.17179*, 2023.
- [14] Z. Geng, A. Pokle, and J. Z. Kolter. One-step diffusion distillation via deep equilibrium models. *Advances in Neural Information Processing Systems*, 36, 2024.
- [15] K. He, X. Zhang, S. Ren, and J. Sun. Deep residual learning for image recognition. In *Proceedings of the IEEE conference on computer vision and pattern recognition*, pages 770–778, 2016.
- [16] J. Ho and T. Salimans. Classifier-free diffusion guidance. *arXiv preprint arXiv:2207.12598*, 2022.
- [17] J. Ho, A. Jain, and P. Abbeel. Denoising diffusion probabilistic models. *Advances in neural information processing systems*, 33:6840–6851, 2020.

- [18] H. Hu, K. C. Chan, Y.-C. Su, W. Chen, Y. Li, K. Sohn, Y. Zhao, X. Ben, B. Gong, W. Cohen, et al. Instruct-imagen: Image generation with multi-modal instruction. *arXiv preprint arXiv:2401.01952*, 2024.
- [19] A. Hyvärinen and P. Dayan. Estimation of non-normalized statistical models by score matching. *Journal of Machine Learning Research*, 6(4), 2005.
- [20] A. Jolicoeur-Martineau, K. Li, R. Piché-Taillefer, T. Kachman, and I. Mitliagkas. Gotta go fast when generating data with score-based models. *arXiv preprint arXiv:2105.14080*, 2021.
- [21] T. Karras, M. Aittala, T. Aila, and S. Laine. Elucidating the design space of diffusion-based generative models. *Advances in Neural Information Processing Systems*, 35:26565–26577, 2022.
- [22] K. Kim, J. Jeong, M. An, M. Ghavamzadeh, K. D. Dvijotham, J. Shin, and K. Lee. Confidence-aware reward optimization for fine-tuning text-to-image models. In *The Twelfth International Conference on Learning Representations*, 2023.
- [23] D. Kingma, T. Salimans, B. Poole, and J. Ho. Variational diffusion models. *Advances in neural information processing systems*, 34:21696–21707, 2021.
- [24] Y. Kirstain, A. Polyak, U. Singer, S. Matiana, J. Penna, and O. Levy. Pick-a-pic: An open dataset of user preferences for text-to-image generation. *Advances in Neural Information Processing Systems*, 36, 2024.
- [25] M. Ku, D. Jiang, C. Wei, X. Yue, and W. Chen. Viescore: Towards explainable metrics for conditional image synthesis evaluation. *arXiv preprint arXiv:2312.14867*, 2023.
- [26] K. Lee, H. Liu, M. Ryu, O. Watkins, Y. Du, C. Boutilier, P. Abbeel, M. Ghavamzadeh, and S. S. Gu. Aligning text-to-image models using human feedback. *arXiv preprint arXiv:2302.12192*, 2023.
- [27] J. Li, D. Li, C. Xiong, and S. Hoi. Blip: Bootstrapping language-image pre-training for unified vision-language understanding and generation. In *ICML*, 2022.
- [28] J. Li, T. Tang, W. X. Zhao, J.-Y. Nie, and J.-R. Wen. Pretrained language models for text generation: A survey. *arXiv preprint arXiv:2201.05273*, 2022.
- [29] T.-Y. Lin, M. Maire, S. Belongie, J. Hays, P. Perona, D. Ramanan, P. Dollár, and C. L. Zitnick. Microsoft coco: Common objects in context. In *Computer Vision—ECCV 2014: 13th European Conference, Zurich, Switzerland, September 6-12, 2014, Proceedings, Part V 13*, pages 740–755. Springer, 2014.
- [30] C. Lu, Y. Zhou, F. Bao, J. Chen, C. Li, and J. Zhu. Dpm-solver: A fast ode solver for diffusion probabilistic model sampling in around 10 steps. *Advances in Neural Information Processing Systems*, 35:5775–5787, 2022.
- [31] C. Lu, Y. Zhou, F. Bao, J. Chen, C. Li, and J. Zhu. Dpm-solver++: Fast solver for guided sampling of diffusion probabilistic models. *arXiv preprint arXiv:2211.01095*, 2022.
- [32] D. Lu and Q. Weng. A survey of image classification methods and techniques for improving classification performance. *International journal of Remote sensing*, 28(5):823–870, 2007.
- [33] Y. Lu, X. Yang, X. Li, X. E. Wang, and W. Y. Wang. Llmscore: Unveiling the power of large language models in text-to-image synthesis evaluation. *Advances in Neural Information Processing Systems*, 36, 2024.
- [34] E. Luhman and T. Luhman. Knowledge distillation in iterative generative models for improved sampling speed. *arXiv preprint arXiv:2101.02388*, 2021.
- [35] S. Luo, Y. Tan, L. Huang, J. Li, and H. Zhao. Latent consistency models: Synthesizing high-resolution images with few-step inference. *arXiv preprint arXiv:2310.04378*, 2023.

- [36] C. Meng, R. Rombach, R. Gao, D. Kingma, S. Ermon, J. Ho, and T. Salimans. On distillation of guided diffusion models. In *Proceedings of the IEEE/CVF Conference on Computer Vision and Pattern Recognition*, pages 14297–14306, 2023.
- [37] T. H. Nguyen and A. Tran. Swiftbrush: One-step text-to-image diffusion model with variational score distillation. *arXiv preprint arXiv:2312.05239*, 2023.
- [38] A. Q. Nichol and P. Dhariwal. Improved denoising diffusion probabilistic models. In *International Conference on Machine Learning*, pages 8162–8171. PMLR, 2021.
- [39] L. Ouyang, J. Wu, X. Jiang, D. Almeida, C. Wainwright, P. Mishkin, C. Zhang, S. Agarwal, K. Slama, A. Ray, et al. Training language models to follow instructions with human feedback. *Advances in Neural Information Processing Systems*, 35:27730–27744, 2022.
- [40] M. Prabhudesai, A. Goyal, D. Pathak, and K. Fragkiadaki. Aligning text-to-image diffusion models with reward backpropagation. *arXiv preprint arXiv:2310.03739*, 2023.
- [41] A. Radford, J. W. Kim, C. Hallacy, A. Ramesh, G. Goh, S. Agarwal, G. Sastry, A. Askell, P. Mishkin, J. Clark, et al. Learning transferable visual models from natural language supervision. In *International conference on machine learning*, pages 8748–8763. PMLR, 2021.
- [42] R. Rafailov, A. Sharma, E. Mitchell, C. D. Manning, S. Ermon, and C. Finn. Direct preference optimization: Your language model is secretly a reward model. *Advances in Neural Information Processing Systems*, 36, 2024.
- [43] R. Rombach, A. Blattmann, D. Lorenz, P. Esser, and B. Ommer. High-resolution image synthesis with latent diffusion models. In *Proceedings of the IEEE/CVF conference on computer vision and pattern recognition*, pages 10684–10695, 2022.
- [44] C. Saharia, W. Chan, S. Saxena, L. Li, J. Whang, E. L. Denton, K. Ghasemipour, R. Gontijo Lopes, B. Karagol Ayan, T. Salimans, et al. Photorealistic text-to-image diffusion models with deep language understanding. *Advances in Neural Information Processing Systems*, 35: 36479–36494, 2022.
- [45] T. Salimans and J. Ho. Progressive distillation for fast sampling of diffusion models. *arXiv preprint arXiv:2202.00512*, 2022.
- [46] A. Sauer, D. Lorenz, A. Blattmann, and R. Rombach. Adversarial diffusion distillation. *arXiv preprint arXiv:2311.17042*, 2023.
- [47] C. Schuhmann, R. Beaumont, R. Vencu, C. Gordon, R. Wightman, M. Cherti, T. Coombes, A. Katta, C. Mullis, M. Wortsman, et al. Laion-5b: An open large-scale dataset for training next generation image-text models. *Advances in Neural Information Processing Systems*, 35: 25278–25294, 2022.
- [48] E. Segalis, D. Valevski, D. Lumen, Y. Matias, and Y. Leviathan. A picture is worth a thousand words: Principled recaptioning improves image generation. *arXiv preprint arXiv:2310.16656*, 2023.
- [49] A. Shih, S. Belkhale, S. Ermon, D. Sadigh, and N. Anari. Parallel sampling of diffusion models. *Advances in Neural Information Processing Systems*, 36, 2024.
- [50] J. Singh and L. Zheng. Divide, evaluate, and refine: Evaluating and improving text-to-image alignment with iterative vqa feedback. *Advances in Neural Information Processing Systems*, 36, 2024.
- [51] J. Sohl-Dickstein, E. Weiss, N. Maheswaranathan, and S. Ganguli. Deep unsupervised learning using nonequilibrium thermodynamics. In *International conference on machine learning*, pages 2256–2265. PMLR, 2015.
- [52] J. Song, C. Meng, and S. Ermon. Denoising diffusion implicit models. *arXiv preprint arXiv:2010.02502*, 2020.
- [53] Y. Song and P. Dhariwal. Improved techniques for training consistency models. *arXiv preprint arXiv:2310.14189*, 2023.

- [54] Y. Song and S. Ermon. Generative modeling by estimating gradients of the data distribution. *Advances in neural information processing systems*, 32, 2019.
- [55] Y. Song, J. Sohl-Dickstein, D. P. Kingma, A. Kumar, S. Ermon, and B. Poole. Score-based generative modeling through stochastic differential equations. *arXiv preprint arXiv:2011.13456*, 2020.
- [56] Y. Song, P. Dhariwal, M. Chen, and I. Sutskever. Consistency models. *International conference on machine learning*, 2023.
- [57] N. Stiennon, L. Ouyang, J. Wu, D. Ziegler, R. Lowe, C. Voss, A. Radford, D. Amodei, and P. F. Christiano. Learning to summarize with human feedback. *Advances in Neural Information Processing Systems*, 33:3008–3021, 2020.
- [58] J. Sun, D. Fu, Y. Hu, S. Wang, R. Rassin, D.-C. Juan, D. Alon, C. Herrmann, S. van Steenkiste, R. Krishna, et al. Dreamsync: Aligning text-to-image generation with image understanding feedback. *arXiv preprint arXiv:2311.17946*, 2023.
- [59] G. Team, R. Anil, S. Borgeaud, Y. Wu, J.-B. Alayrac, J. Yu, R. Soricut, J. Schalkwyk, A. M. Dai, A. Hauth, et al. Gemini: a family of highly capable multimodal models. *arXiv preprint arXiv:2312.11805*, 2023.
- [60] A. K. Vijayakumar, M. Cogswell, R. R. Selvaraju, Q. Sun, S. Lee, D. Crandall, and D. Batra. Diverse beam search: Decoding diverse solutions from neural sequence models. *arXiv preprint arXiv:1610.02424*, 2016.
- [61] P. von Platen, S. Patil, A. Lozhkov, P. Cuenca, N. Lambert, K. Rasul, M. Davaadorj, and T. Wolf. Diffusers: State-of-the-art diffusion models. <https://github.com/huggingface/diffusers>, 2022.
- [62] B. Wallace, M. Dang, R. Rafailov, L. Zhou, A. Lou, S. Purushwalkam, S. Ermon, C. Xiong, S. Joty, and N. Naik. Diffusion model alignment using direct preference optimization. *arXiv preprint arXiv:2311.12908*, 2023.
- [63] B. Wallace, M. Dang, R. Rafailov, L. Zhou, A. Lou, S. Purushwalkam, S. Ermon, C. Xiong, S. Joty, and N. Naik. Diffusion model alignment using direct preference optimization. *arXiv preprint arXiv:2311.12908*, 2023.
- [64] X. Wu, Y. Hao, K. Sun, Y. Chen, F. Zhu, R. Zhao, and H. Li. Human preference score v2: A solid benchmark for evaluating human preferences of text-to-image synthesis. *arXiv preprint arXiv:2306.09341*, 2023.
- [65] X. Wu, K. Sun, F. Zhu, R. Zhao, and H. Li. Human preference score: Better aligning text-to-image models with human preference. In *Proceedings of the IEEE/CVF International Conference on Computer Vision*, pages 2096–2105, 2023.
- [66] J. Xu, X. Liu, Y. Wu, Y. Tong, Q. Li, M. Ding, J. Tang, and Y. Dong. Imagereward: Learning and evaluating human preferences for text-to-image generation. *Advances in Neural Information Processing Systems*, 36, 2024.
- [67] J. Yu, Y. Xu, J. Y. Koh, T. Luong, G. Baid, Z. Wang, V. Vasudevan, A. Ku, Y. Yang, B. K. Ayan, et al. Scaling autoregressive models for content-rich text-to-image generation. *arXiv preprint arXiv:2206.10789*, 2(3):5, 2022.
- [68] K. Zhang, X. Yang, W. Y. Wang, and L. Li. Redi: Efficient learning-free diffusion inference via trajectory retrieval. *arXiv preprint arXiv:2302.02285*, 2023.
- [69] Q. Zhang and Y. Chen. Fast sampling of diffusion models with exponential integrator. *arXiv preprint arXiv:2204.13902*, 2022.
- [70] Y. Zhang, E. Tzeng, Y. Du, and D. Kislyuk. Large-scale reinforcement learning for diffusion models. *arXiv preprint arXiv:2401.12244*, 2024.
- [71] H. Zheng, P. He, W. Chen, and M. Zhou. Truncated diffusion probabilistic models and diffusion-based adversarial auto-encoders. *arXiv preprint arXiv:2202.09671*, 2022.

- [72] H. Zheng, W. Nie, A. Vahdat, K. Azizzadenesheli, and A. Anandkumar. Fast sampling of diffusion models via operator learning. In *International Conference on Machine Learning*, pages 42390–42402. PMLR, 2023.
- [73] D. M. Ziegler, N. Stiennon, J. Wu, T. B. Brown, A. Radford, D. Amodei, P. Christiano, and G. Irving. Fine-tuning language models from human preferences. *arXiv preprint arXiv:1909.08593*, 2019.

Appendix



Figure 8: Samples from our RG-LCM (HPSv2.1) with the teacher Stable Diffusion v2.1-base. The resolution is 512 x 512.

In the main paper, we distill our RG-LCD from the Stable Diffusion-v2.1 (768 x 768) [43]. Fig. 8 further shows the samples from our RG-LCM (HPSv) distilled from Stable Diffusion-v2.1-base (512 x 512) [43]. The rest of the appendix is structured as below

- Appendix A details the experimental setup and hyperparameter configurations.
- Appendix B elaborates on the training processes and sampling techniques from a (latent) CM.
- Appendix C shows extra samples generated by various models.

	CLIPScore	PickScore	ImageReward	HPSv2.1
β	5.0	5.0	1.0	1.0

Table 2: β for different RG-LCMs when training with different RMs.

A Additional Experimental Details and Hyperparameters (HPs)

For qualitative evaluation, we ensure consistency across all methods by using the same random seed for head-to-head image comparisons.

As mentioned in Sec. 5, our training are conducted on the CC12M datasets [6], as the LAION-Aesthetics datasets [47] used in the original LCM paper [35] are not accessible². We train all LCMs (including RG-LCMs and the standard LCM) by distilling from the teacher LDM Stable Diffusion-v2.1 [43] for 10K gradient steps on 8 NVIDIA A100 GPUs. When learning the standard LCM, we use a batch size 32 on each GPU (256 effective batch size). For RG-LCMs, we use a batch size 5 on each GPU (40 effective batch size). Interestingly, we observe that different batch sizes do not impact the final performance too much.

We use the same set of hyperparameters (HP) for training RG-LCM and the standard LCM by following the settings listed in the diffusers [61] library, except that RG-LCM has a unique HP β . Specifically, we set the learning rate $1e-6$, EMA rate $\mu = 0.95$ and the guidance scale range $[\omega_{\min}, \omega_{\max}] = [5, 15]$. We include more training details in Appendix A. Following the practice in [35], we initialize f_θ with the same parameters as the teacher LDM. We further encode the CFG scale ω by applying the Fourier embedding to ω and integrate it into the LCM backbone by adding the projected ω -embedding into the original embedding as in [36].

As mentioned in Sec. 3.3, we use DDIM [52] as our ODE solver Ψ with a skipping step $k = 20$, the formula of the DDIM ODE solver Ψ_{DDIM} from t_{n+k} to t_n is given below [35]

$$\Psi_{\text{DDIM}}(\mathbf{z}_{t_{n+k}}, t_{n+k}, t_n, \mathbf{c}) = \underbrace{\frac{\alpha_{t_n}}{\alpha_{t_{n+k}}} \mathbf{z}_{t_{n+k}} - \beta_{t_n} \left(\frac{\beta_{t_{n+k}} \cdot \alpha_{t_n}}{\alpha_{t_{n+k}} \cdot \beta_{t_n}} - 1 \right) \hat{\mathbf{e}}_\psi(\mathbf{z}_{t_{n+k}}, \mathbf{c}, t_{n+k})}_{\text{DDIM Estimated } \mathbf{z}_{t_n}} - \mathbf{z}_{t_{n+k}}, \quad (13)$$

where $\hat{\mathbf{e}}_\psi$ denotes the noise prediction model from the teacher LDM. α_{t_n} and β_{t_n} specify the noise schedule. For the forward process SDE defined in (1), we have

$$\boldsymbol{\mu}(t) = \frac{d \log \alpha(t)}{dt}, \quad \sigma^2(t) = \frac{d\beta^2(t)}{dt} - 2 \frac{d \log \alpha(t)}{dt} \beta^2(t). \quad (14)$$

As a result, we have $p_t(\mathbf{x}_t) = \mathcal{N}(\mathbf{x}_t | \alpha(t), \beta^2(t)\mathbf{I})$. We refer interested readers to the original LCM paper [35] for further details.

Reward scale β for different RG-LCMs with different RMs. In Sec. 5.1 and 5.2, we train our RG-LCMs with different RMs, including CLIPScore [41], PickScore [24], ImageReward [66] and HPSv2.1 [64]. Table 2 shows the β we used for different RMs when obtaining the results in Fig. 4, 5 and Table 1.

Details for integrating an LRM into RG-LCM As discussed in Sec. 4.2, the LRM admits a similar architecture as the CLIP [41] model, with the distinction of replacing the visual encoder with a latent encoder. We retain the original pretrained text encoder and focus on pretraining the latent encoder from scratch. This process mirrors the CLIP’s pretraining approach, minimizing the same contrastive loss on the CC12M datasets [6]. The image latent is extracted with the same VAE encoder used in the teacher LDM Stable Diffusion-v2.1. Upon completing the pretraining phase, the LRM demonstrates promising initial results, achieving a zero-shot Top-1 Accuracy of 38.8% and Top-5 Accuracy of 66.47% on the ImageNet validation set [9]. These metrics underscore the model’s fundamental capability in understanding text-image alignments.

During the RG-LCD process, we finetune the LRM to match the preference of an expert RM. We train the last 2 layer of the latent encoder and the last 5 layers of the text encoder. We set the learning

²<https://laion.ai/notes/laion-maintenance>

rate to 0.0000033 following [64]. Note that we do not perform heavy HP searches to determine their optimal values.

B Training and Sampling from (Latent) CM

B.1 Multistep sampling from a learned CM and LCM

We provide the pseudo-codes for multistep consistency sampling [56] and multistep latent consistency sampling [35] procedures in Algorithm 1 and Algorithm 2, respectively. The multistep sampling procedures alternate between the consistency mapping and noise-injection steps, trading additional computation resources for better sample quality. In the n -th iteration, we first perturb the predicted sample \mathbf{x} (or \mathbf{z}) with Gaussian noise to obtain $\hat{\mathbf{x}}_{\tau_n}$ (or $\hat{\mathbf{z}}_{\tau_n}$). We then map the noisy sample $\hat{\mathbf{x}}_{\tau_n}$ (or $\hat{\mathbf{z}}_{\tau_n}$) to obtain a new \mathbf{x} (or \mathbf{z}).

Algorithm 1 Multistep Consistency Sampling

Require: CM f_θ , steps N , timestep sequence $\tau_1 > \tau_2 > \dots > \tau_{N-1}$, noise schedule $\alpha(t), \beta(t)$.
 Sample initial noise $\hat{\mathbf{x}}_T \sim \mathcal{N}(\mathbf{0}, \mathbf{I})$
 $\mathbf{x} \leftarrow f_\theta(\hat{\mathbf{x}}_T, T)$
for $n = 1, \dots, N - 1$ **do**
 Sample $\hat{\mathbf{x}}_{\tau_n} \sim \mathcal{N}(\alpha(\tau_n)\mathbf{x}, \beta^2(\tau_n)\mathbf{I})$
 $\mathbf{x} \leftarrow f_\theta(\hat{\mathbf{x}}_{\tau_n}, \tau_n)$
end for
Return \mathbf{x}

Algorithm 2 Multistep Latent Consistency Sampling

Require: LCM f_θ , steps N , timestep sequence $\tau_1 > \tau_2 > \dots > \tau_{N-1}$, noise schedule $\alpha(t), \beta(t)$, text prompt \mathbf{c} , CFG scale ω , VAE decoder \mathcal{D} .
 Sample initial noise $\hat{\mathbf{z}}_T \sim \mathcal{N}(\mathbf{0}, \mathbf{I})$
 $\mathbf{z} \leftarrow f_\theta(\hat{\mathbf{z}}_T, \omega, \mathbf{c}, T)$
for $n = 1, \dots, N - 1$ **do**
 Sample $\hat{\mathbf{z}}_{\tau_n} \sim \mathcal{N}(\alpha(\tau_n)\mathbf{z}, \beta^2(\tau_n)\mathbf{I})$
 $\mathbf{z} \leftarrow f_\theta(\hat{\mathbf{z}}_{\tau_n}, \omega, \mathbf{c}, T)$
end for
Return $\mathcal{D}(\mathbf{z})$

B.2 Training procedures of RG-LCD

Algorithm 3 Reward Guided Latent Consistency Distillation

Require: dataset \mathcal{D} , initial model parameter θ , learning rate η , ODE solver Ψ , distance metric d , EMA rate μ , noise schedule $\alpha(t), \beta(t)$, guidance scale $[\omega_{\min}, \omega_{\max}]$, skipping interval k , VAE encoder \mathcal{E} , **decoder \mathcal{D} , reward model \mathcal{R} , reward scale β**
 Encoding training data into latent space: $\mathcal{D}_z = \{(\mathbf{z}, \mathbf{c}) \mid \mathbf{z} = E(\mathbf{x}), (\mathbf{x}, \mathbf{c}) \in \mathcal{D}\}$
 $\theta^- \leftarrow \theta$
repeat
 Sample $(\mathbf{z}, \mathbf{c}) \sim \mathcal{D}_z, n \sim \mathcal{U}[1, N - k]$ and $\omega \sim [\omega_{\min}, \omega_{\max}]$
 Sample $\mathbf{z}_{t_{n+k}} \sim \mathcal{N}(\alpha(t_{n+k})\mathbf{z}; \sigma^2(t_{n+k})\mathbf{I})$
 $\hat{\mathbf{z}}_{t_n}^{\Psi, \omega} \leftarrow \mathbf{z}_{t_{n+k}} + (1 + \omega)\Psi(\mathbf{z}_{t_{n+k}}, t_{n+k}, t_n, \mathbf{c}) - \omega\Psi(\mathbf{z}_{t_{n+k}}, t_{n+k}, t_n, \emptyset)$
 $J(\theta) \leftarrow \mathcal{R}(\mathcal{D}(f_\theta(\mathbf{z}_{t_{n+k}}, \omega, \mathbf{c}, t_{n+k})), \mathbf{c})$
 $\mathcal{L}(\theta, \theta^-; \Psi) \leftarrow d(f_\theta(\mathbf{z}_{t_{n+k}}, \omega, \mathbf{c}, t_{n+k}), f_{\theta^-}(\hat{\mathbf{z}}_{t_n}^{\Psi, \omega}, \omega, \mathbf{c}, t_n)) - \beta \cdot J(\theta)$
 $\theta \leftarrow \theta - \eta \nabla_\theta \mathcal{L}(\theta, \theta^-)$
 $\theta^- \leftarrow \text{stop_grad}(\mu\theta^- + (1 - \mu)\theta)$
until convergence

Algorithm 3 presents the pseudo-codes for our RG-LCD. We use the red color to highlight the difference between our RG-LCD and the standard LCD [35].

C Additional Qualitative Results

We provide additional samples from our RG-LCMs with different RMs compared with the baseline LCM and teacher Stable Diffusion v2.1 in Fig. 9 and 10.

The prompts for images in Fig. 9 in the left-to-right order are given below

- Van Gogh painting of a teacup on the desk
- Impressionist painting of a cat, textured, hypermodern
- photo of a kid playing , snow filling the air
- A fluffy owl sits atop a stack of antique books in a detailed and moody illustration.
- a deer reading a book
- a photo of a monkey wearing glasses in a suit

The prompts for images in Fig. 10 in the left-to-right order are given below

- ornate archway inset with matching fireplace in room
- Poster of a mechanical cat, technical Schematics viewed from front
- portrait of a person with Cthulhu features, painted by Bouguereau.
- a serene nighttime cityscape with lake reflections, fruit trees
- Teddy bears working on new AI research on the moon in the 1980s.
- A cinematic shot of robot with colorful feathers

Fig. 11 presents image samples when integrating a latent proxy RM (LRM) into our RG-LCD procedures. The prompts in the left-to-right order are given below

- a man in a brown blazer standing in front of smoke, backlit, in the style of gritty hollywood glamour, light brown and emerald, movie still, emphasis on facial expression, robert bevan, violent, dappled
- a cute pokemon resembling a blue duck wearing a puffy coat
- Highly detailed photograph of a meal with many dishes.

Fig. 12 includes additional samples for the ablation on the reward scale β . The prompts in the top-to-bottom order are given below

- Ultra realistic photo of a single light bulb, dramatic lighting
- Pirate ship trapped in a cosmic maelstrom nebula
- A golden retriever wearing VR goggles.
- Highly detailed portrait of a woman with long hairs, stephen bliss, unreal engine, fantasy art by greg rutkowski.
- A stunning beautiful oil painting of a lion, cinematic lighting, golden hour light.
- A raccoon wearing a tophat and suit, holding a briefcase, standing in front of a city skyline.



Figure 9: Samples from our RG-LCMs with different RMs compared with the baseline LCM and teacher Stable Diffusion v2.1.

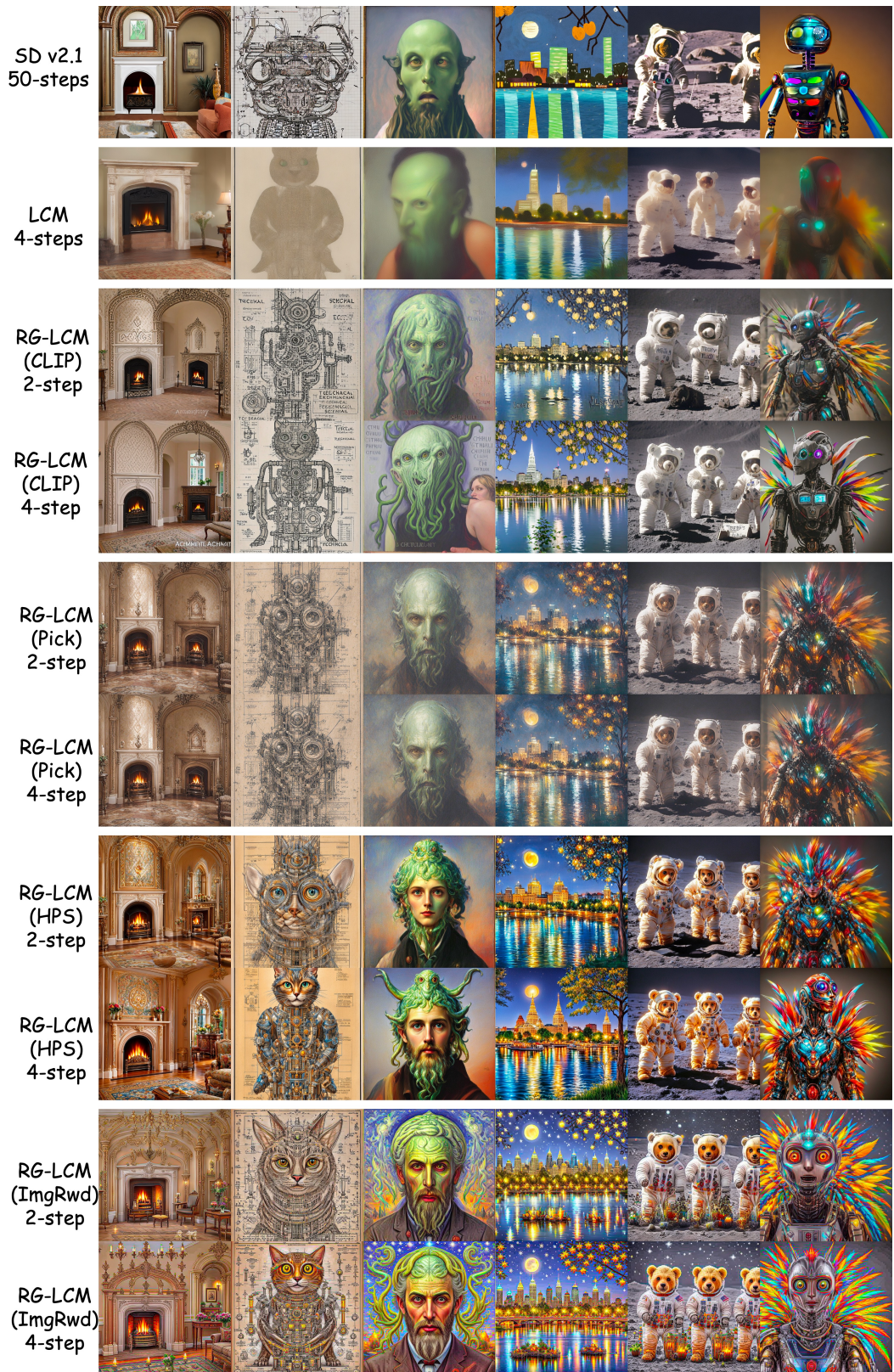


Figure 10: More samples from our RG-LCMs with different RMs compared with the baseline LCM and teacher Stable Diffusion v2.1.

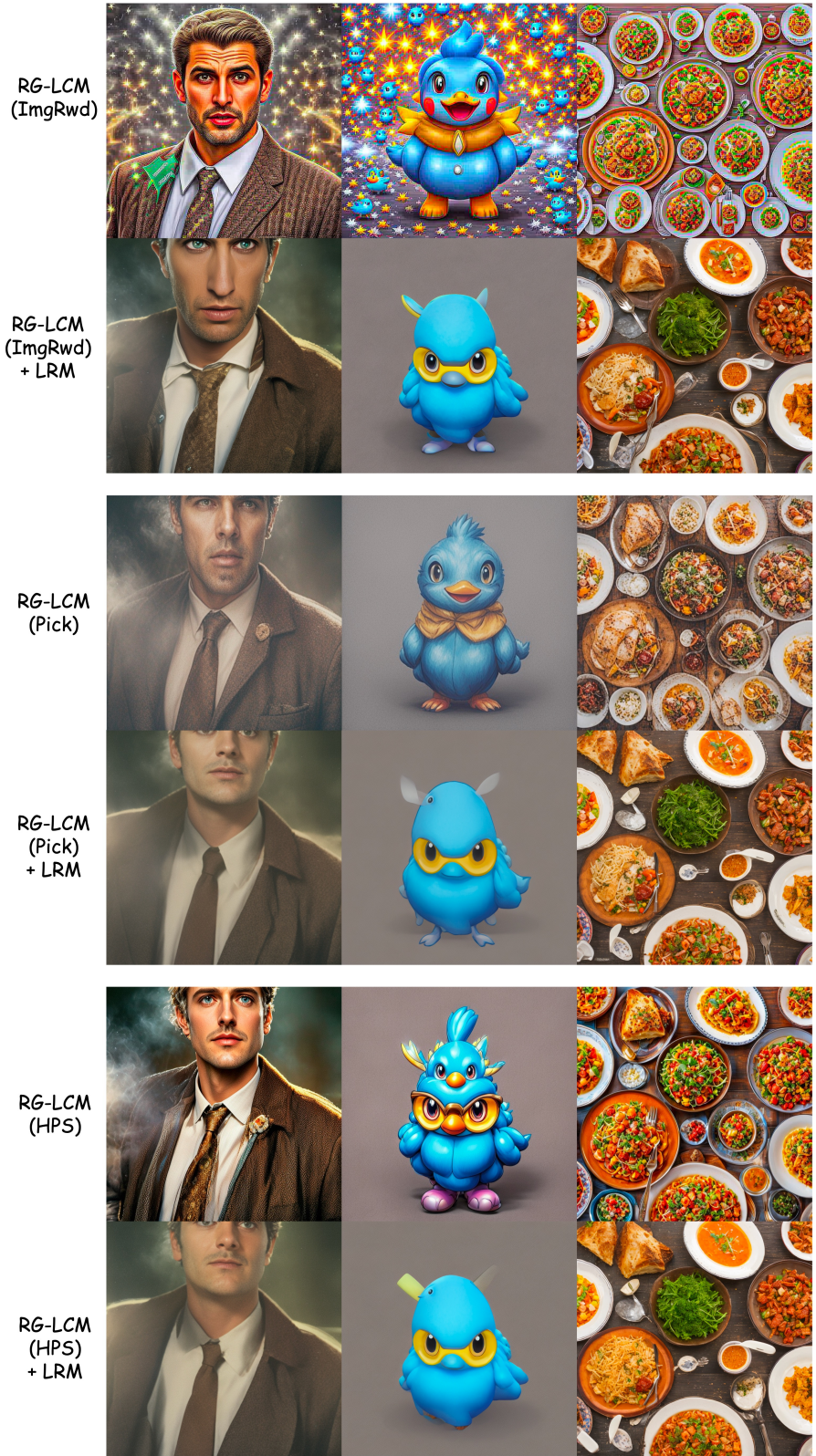


Figure 11: Effect of the Latent proxy RM (LRM). Integrating the LRM into our RG-LCD procedures makes the generated images natural, corresponding to the lower FID in Table 1. Moreover, it helps eliminate the high-frequency noise in the generated images.

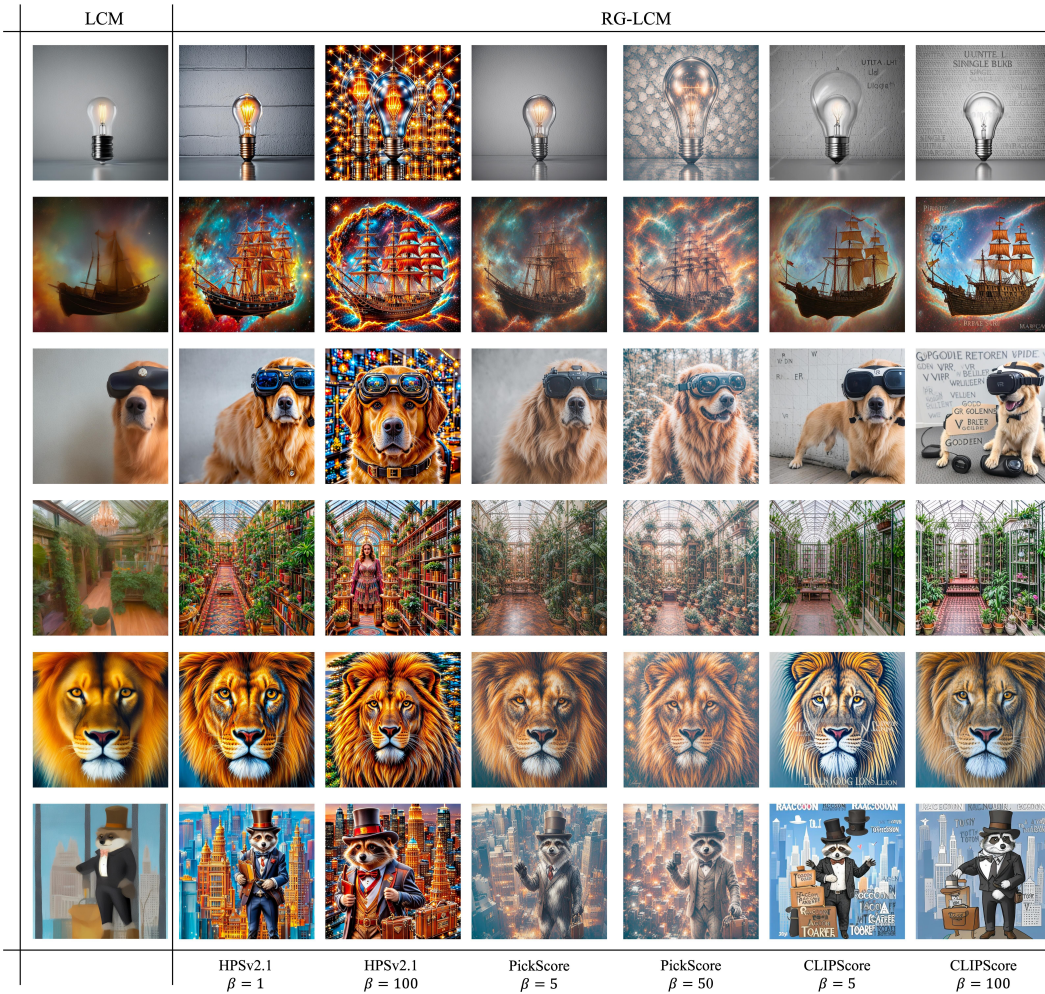


Figure 12: Additional images to study the impact of the reward scale β . We generate all samples with 4 steps.